

Macroscopic Salt Rejection through Electrostatically Gated Monolayer Porous Graphene

Roman M. Wyss,^{†,§} Tian Tian,^{‡,§} Khadija Yazda,[¶] Hyung Gyu Park,[¶] and
Chih-Jen Shih^{*,‡}

[†]*Institute of Soft Materials Department of Material Sciences, Eidgenössische Technische
Hochschule (ETH) Zürich, Vladimir-Prelog-Weg 1-5, Zürich CH-8093, Switzerland.*

[‡]*Institute for Chemical and Bioengineering Department of Chemistry and Applied Biosciences,
Eidgenössische Technische Hochschule (ETH) Zürich, Vladimir-Prelog-Weg 1-5, Zürich
CH-8093, Switzerland.*

[¶]*Nanoscience for Energy Technology and Sustainability, Department of Mechanical and Process
Engineering, Eidgenössische Technische Hochschule (ETH) Zürich, Tannenstrasse 3, Zürich
CH-8092, Switzerland.*

[§]*R. M. S. and T. T. contributed equally to this work*

E-mail: chih-jen.shih@chem.ethz.ch

Abstract

Atomically thin graphene nanopores is emerging as one of the most promising candidates for next-generation membrane technology owing to the ultrahigh permeability. However, the size-exclusive mechanism limits its scalability as it remains technically challenging to drill subnanometer pores over a large area. Here we report macroscopic salt rejection through monolayer porous graphene with the pore sizes of 20 ± 10 nanometers, overcoming the pore size limitation set by the hydrated radii. By electrostatically gating a sheet of porous graphene, we report a considerable reduction of salt flux by up to 55% with the gate voltage. We systematically investigate the effects of salt concentration and species, including developing a theory to model the electrolyte diffusion through a nanopore in a sheet of gated monolayer graphene. The interplay between graphene quantum capacitance and electrical double layer is identified to be the main mechanism responsible for the observed salt rejection, when the pore size is comparable to the Debye screening length. Our findings reveal a new degree of freedom controlling the membrane potential and electrolyte permeation through porous two-dimensional monolayers.

Introduction

A central objective in the emerging field of nanofluidics is to manipulate transport phenomena at nanometer scale to enable new technological opportunities for sensing and energy applications. The reduction of characteristic dimensions in nanofluidics gives rise to substantially different transport properties compared to their bulk counterparts.¹ In nanopores, for example, the effect of surface-mediated transport becomes dominant when the pore size is comparable to the solute diffusion length, enabling new applications, including ionic diodes,² field-effect transistors,³ desalination,⁴ and nanopore-based DNA sequencing.^{5,6} Porous, atomically thin two-dimensional (2D) materials, such as graphene, embody an ideal membrane materials due to their ultimate permeability.⁷⁻¹¹ Early research has suggested that using nanoporous graphene as the desalination membrane enables excellent salt rejection by preventing the permeation of the hydrated ions the (1 nm - 3 nm) with simultaneous high water permeation.¹²⁻¹⁷ Nevertheless, the fabrication of sub-5 nanometer porous 2D membranes over a large area with atomic precision is technically challenging.^{13,18-20} Moreover, a small portion of large pores can significantly diminish salt rejection. Accordingly, recent research efforts have explored the effect of surface charges on the selectivity of ion transport, as a consequence of coulombic repulsion of the solvated ion and the charged functional groups on graphene.^{18,21} However, it remains controversial that if the surface charges can result in a degree of salt rejection, as the membrane potential is sensitive to the surroundings and chemical treatment.²² The difficulty in turn hinders fundamental understanding of the interactions between the atomically thin 2D membrane and electrolyte solution. Here, we demonstrate macroscopic salt rejection through a sheet of large-area porous graphene using electrostatic gating, thereby deepening the understanding of ion-graphene interaction and its implications on nanoporous graphene-based desalination applications.

Results and discussions

Free diffusion through porous graphene

Fig. 1a depicts the experimental setup characterizing ionic diffusion through a sheet of monolayer porous graphene (PG). Two reservoirs, namely the high-concentration reservoir (HCR) containing electrolyte solution with molar concentration c_0 , and the low-concentration reservoir (LCR) containing de-ionized (DI) water, are separated by a PG membrane supported by polycarbonate track-etched (PCTE) film. Magnetic stirrers are used to minimize the effects of external concentration polarization, and a conductivity probe is placed in the LCR to monitor the ionic concentration as a function of time. The membrane is attached to a piece of copper tape connected to a voltage source applying an electrical bias V_G , with the LCR grounded (Fig. 1a inset). We fabricated the PCTE-supported PG using the protocol developed by our group,²³ as schematically shown in Fig. 1b. The normally distributed, circular pores with pore diameters of 20 ± 10 nm (Fig. 1c inset) over a large area were drilled on graphene. By optimizing the subsequent transfer process, a high surface coverage ($> 98\%$) of graphene on PCTE was reached (Fig. 1c), allowing to reliably characterize the ion transport behavior (details see Supplementary Information Section S1). The system presented here allows us to systematically investigate the diffusive flux across a sheet of porous graphene, J , driven by the gradient of electrochemical potential in the electrolyte medium.

First, the control experiments were carried out by measuring the ionic diffusion of seven salt species, including KCl, NaCl, LiCl, K_2SO_4 , $MgSO_4$, $CaCl_2$ and $K_3Fe(CN)_6$, through the bare PCTE membrane at $c_0 = 0.1$ mM. As the diffusive flux is comparably small, the conductivity versus time profile (e.g. Fig. 2a) remains linear within the measurement duration (1 h), suggesting the concentration change in individual reservoirs is negligible

Isn't the increasing of conductivity a measure of the diffusion of ions?

. The diffusive fluxes correspond to different salts were obtained by converting the conductivity-time profiles with the calibration curves (blue bars in Fig. 2b and Supplementary Fig. S2). For comparison purposes, based on the assumption that the membrane consists cylindrical pores with

uniform diameter and a low tortuosity τ of ~ 1.2 ,¹⁹ the molar diffusive flux through the bare PCTE membrane, J_{PCTE} , follows:

$$J_{\text{PCTE}} = \frac{\pi a^2 N_p D \Delta c}{\delta \tau} \quad (1)$$

where a is the PCTE pore radius, N_p is numbers of pore per area, D is the salt diffusivity, and Δc is the bulk concentration difference between two reservoirs, i.e., $\Delta c \sim c_0$, δ is the thickness of the PCTE membrane, and τ is the tortuosity. By using the salt diffusivity values provided by the PTCE vendor (Supplementary Table S1), the calculated diffusive fluxes (red bars in Fig. 2b) show reasonable agreement with the experimental values.

Next, we carried out the same experiments using the PG-covered PCTE membrane (PG-PCTE), without electrostatic gating. The measured diffusive flux values, J_{PG0} (green bars in Fig. 2b), remain at the same order of magnitude compared to those of bare PCTE membrane, suggesting that the mass transfer resistance of PG is not significant, as the permeability is high. We observed a more pronounced decrease of diffusive flux in KCl, K₂SO₄ and K₃Fe(CN)₆ systems but not for the rest of the salts. We hypothesized that the strong cation- π interactions between K⁺ cations and graphene slow down the migration of cations along the surface-mediated transport pathway.²⁴

Salt rejection induced by electrostatic gating

We next discuss the effects of electrostatic gating on graphene. In order to avoid any interference from the conductivity probe to the membrane potential, the “three-interval” method, which had been used in controlling the membrane potential in mesoporous carbon membranes,²¹ is adopted here. Fig. 2a presents the representative data of the measured conductivity with respect to time. Specifically, in the first interval, the gate voltage source is turned off and the conductivity probe is on, allowing us to obtain the conductivity-time profile corresponding to the diffusive flux through the PG-PCTE membrane, giving the average slope s_1 . In the second interval, a voltage V_G is applied to the membrane after turning off the conductivity probe, followed by the third interval, in which the conductivity probe is turned on again to give the corresponding slope, s_3 . The slope

corresponding to the second interval, s_2 , as the conductivity probe is off, is determined by linearly interpolating the conductivities from the endpoint of interval 1 to the starting point of interval 3. Accordingly, we define the salt rejection factor, ξ , which is effectively equivalent to the relative degree of diffusive flux decrease as follows:

$$\xi = \frac{\bar{s} - s_2}{\bar{s}} = \frac{J_{PG0} - J_{PG}(V_G)}{J_{PG0}} \quad (2)$$

where \bar{s} is the average slope of s_1 and s_3 , namely $(s_1 + s_3)/2$, and $J_{PG}(V_G)$ is the diffusive flux across the PTCE-supported PG double layer as a function of V_G . Note that a positive ξ between 0 and 1 represents a decrease of the diffusive flux. The factor ξ enables a reliable and stable measurement of salt rejection, as the salt species and initial conditions may induce a degree of measurement uncertainty between different samples. A control experiment was performed to ensure the copper tape was not in direct contact with the ionic solution (Supplementary Section 3).

Using 0.1 mM KCl solution in HCR, we measured ξ as a function of V_G within ± 1.25 V, before triggering the electrochemical reactions (Fig. 2c). We observe an asymmetric dependence of ξ with respect to V_G , with a higher degree of salt rejection for $V_G > 0$, where positive carriers (holes) are induced in graphene. We notice that an increase ξ , or a decrease of J_{PG} with V_G , showing an inverse trend compared to those observed in ionic field effect transistors (IFETs), in which the diffusive flux increases with the gate voltage.^{3,25} A further increase of the KCl concentration c_0 influences the attainable degree of salt rejection. ξ values measured at $V_G = 1.25$ V, ξ_{\max} , as a function of c_0 from 10^{-4} to 10^{-2} M KCl (see Supplementary Section S4) exhibit a power law dependency (Fig. 2d). The $\xi_{\max} - c_0$ relation can be nicely fitted by a power law function following $\xi_{\max} c_0^{0.59} = \text{Constant}$. As the Debye screening length in solution, λ_D , is inversely proportional to $c^{0.5}$, we infer that the V_G -induced salt rejection originates from the modulation of the electrical double layer (EDL), as will be discussed later.

Self-consistent ion transport theory

In order to quantitatively understand the observed V_G dependence, we develop a theory to model the coupling of graphene's elementary transport properties and EDL, in order to quantify the ionic transport through a graphene nanopore. Under the assumption that the time scale for the bulk concentration change is significantly longer than that of ionic diffusion, the pseudo-steady state approximation holds. Accordingly, the steady-state Nernst-Planck equation describing the ionic transport in an electrolyte solution is given by:²⁶

$$\nabla \cdot \mathbf{J}_i = -\nabla \cdot \left(\frac{D_i}{k_B T} c_i N_A \nabla \mu_i \right) = 0 \quad (3)$$

where \mathbf{J} is the mass flux, subscript i corresponds to the species (anion or cation), D is the diffusivity, k_B is the Boltzmann constant, T is temperature, c is the molar concentration, N_A is the Avogadro constant, and μ_i is the electrochemical potential. Under the assumption of ideal solution, it follows:²⁷

$$\nabla \mu_i = k_B T \nabla \ln x_i + z_i e \nabla \psi \quad (4)$$

where x is the molar fraction, z is the ionic valence, e is the unit charge, and ψ is the electric potential. On the other hand, the Poisson equation describing the electric potential distribution is given by:

$$\nabla \cdot (\varepsilon_m \varepsilon_0 \nabla \psi) = -N_A e \sum_i c_i z_i \quad (5)$$

where ε_m is the relative permittivity of individual materials in the system. Including water and the internal Stern layer,²⁸ and ε_0 is the vacuum permittivity. When applying V_G to graphene adjacent to the electrolyte solution, charges (electrons or holes) are induced in graphene; the electroneutrality of the entire system suggests:

$$\sigma_G S_G + \sum_i \int_{\Omega} z_i c_i N_A e d^3 \Omega = 0 \quad (6)$$

where σ_G is the charge density in graphene, S_G is the total area of graphene, and Ω corresponds to the entire volumetric domain of electrolyte solution. Note that the graphene surface potential, ψ_G , is not equivalent to V_G due to the graphene quantum capacitance effect²⁹ (Fig. 3a) following:

$$V_G = \Delta\phi_G + \psi_G \quad (7)$$

where $\Delta\phi_G$ is the change of graphene's work function. Under the assumption that the charge neutrality point of graphene coincides with the Dirac point at $V_G = 0$, the elementary electronic properties of graphene give:

$$\Delta\phi_G = \text{sign}(\sigma_G) \frac{\hbar v_F}{e} \sqrt{\frac{\pi |\sigma_G|}{e}} \quad (8)$$

where \hbar is the reduced Planck constant, and $v_F = 1.1 \times 10^6 \text{ m}\cdot\text{s}^{-1}$ is the Fermi velocity of graphene (more details find Supplementary Section S5). Note that the PG film fabricated experimentally is double-layer turbostratic graphene, in which we assume the $\Delta\phi_G - \sigma_G$ dependence follows Eq. 8. The theory proposed here was solved self-consistently by discretizing Eqs. 3-5 using the finite-element method (FEM), in which the graphene surface potential is coupled with Eqs. 6-8 that were solved simultaneously to reach convergent numerical solutions of σ_G and ψ_G for a given V_G . Clearly, the above model yields symmetric characteristics for σ_G and ψ_G with respect to V_G due to the symmetric band structure of graphene (Eq. 8). However, for graphene synthesized by chemical vapor deposition (CVD) used in our experiments, it is well-recognized that the electron traps are inherently introduced during synthesis and patterning,³⁰ effectively reducing the charge density and surface potential on graphene $V_G < 0$ (Supplementary Fig. S3). With the nonideality in mind, hereafter, we compare the calculations and experiments in the regime of $V_G > 0$. For example, Fig. 3c presents the calculated σ_G and ψ_G as a function of V_G considering the ionic diffusion through a single 20 nm-diameter nanopore drilled on a sheet of semi-infinite double layer graphene that separates HCR containing KCl solution at $c_0 = 0.1 \text{ mM}$, and LCR at $c_0/10$ in axisymmetric coordinates (details see Supplementary Section S5). Indeed, the interplay between

graphene quantum capacitance and the EDL significantly reduces the graphene surface potential ψ_G to ~ 0.3 V at $V_G = 1.25$ V, corresponding a surface charge density σ_G of ~ 0.08 C·m⁻². Note that as we mentioned earlier, an important merit of the system here is that the surface charge density can be precisely determined and controlled, rather than being treated as a fitting parameter as in most of the 2D nanopore studies.¹⁸

Salt rejection mechanism

The numerical procedure described above allows us to resolve the concentration and electric potential profiles near to a graphene nanopore for a given V_G . Since the ionic flux is driven by both ψ and c fields (see Eq. 3 and 4), we focus on the electrochemical potential μ_i , which represents the combined driving force, to reveal its dependence on the applied V_G . Following the same system considered in Fig. 3b, the calculated axisymmetric electric potential ψ and the relative electrochemical potentials, $\Delta\mu_{K^+}$ and $\Delta\mu_{Cl^-}$, for $V_G = 0.75$ V are shown in Fig. 4a and 4b, respectively. The reference point of the electrochemical potentials is set at the bulk phase in the HCR. As expected, the electric potential reaches the maximum at the graphene surface (with ψ_G of ~ 100 mV) and decays towards the bulk solution phase, forming an EDL surrounding the graphene surface. Since the Debye screening length λ_D is comparable to the pore radius R_G , the electric potential at the nanopore center remains at ~ 25 mV, comparable to the thermal energy at room temperature ($k_B T = 26$ meV). Consequently, it is evident that the potential barrier is sufficient to modulate the diffusive flux.

We further reveal the cation and anion transport pathways by looking into their electrochemical potentials (Fig. 4b). By increasing V_G , a more positive ψ_G on graphene surface reduces the cation concentration at the pore edge due to the electrostatic interactions, thereby increasing its concentration gradient at the pore center. On the other hand, the anion concentration near the pore edge increases exponentially, such that the concentration gradient at the pore center becomes small. (also see Supplementary Fig.s S4). We also observe that $\Delta\mu_+$ is dominated by the concentration, while $\Delta\mu_-$ is much less than $\Delta\mu_+$ due to the balance between the diffusion and drift potentials

(see Supplementary Fig. S5). The observations confirm the distinct ionic transport pathways upon applying a positive V_G : pore center for cations and pore edge for anions. Fig. 4c presents the calculated z-component of the cation and anion fluxes through the pore at the graphene plane ($z = 0$), J_z , as a function of the normalized radius, r/R_G , where r is the radial coordinate and R_G is the pore radius, at different V_G values. Note that J_z is negative because the LCR is placed at $z \leq 0$ in the simulations. At $V_G = 0$ (pure diffusion), the anion and cation flux profiles are identical, with a higher flux near the pore edge, which is expected, as the concentration gradient is higher. By gradually increasing V_G , both fluxes are reduced throughout the pore, while the degree of reduction is more pronounced at the pore edge for the cation, and at the pore center for the anion, following the scenarios we discussed above. Accordingly, the integrated fluxes across the pore, $|J_z|$, are reduced with V_G (Fig. 4d). A total flux reduction of up to 80% is predicted. Another interesting finding here is that, by increasing V_G , the nanopore transport preferentially allows cations over anions, or in other words, the anion flux is more reduced with V_G (see Fig. 4c), known as the ion selectivity of graphene nanopore.¹⁸

The above mechanistic findings, nevertheless, do not fully clarify the experimentally observed reduction of diffusive flux upon gating. Indeed, the same physical mechanism also governs the ionic transport through an IFET, in which a nonzero electric potential at the nanopore center usually results in an increase of ionic conductivity.^{3,31,32} To this end, we further increased the graphene surface potential ψ_G considering the same system (Supplementary Section 6). Intriguingly, by increasing ψ_G larger than 400 mV, the ionic flux starts to increase, reversing the trend observed at the low ψ_G regime, due to (i) the drift flux become dominant over diffusion flux and (ii) the concentration near the pore edge (preferred path) greatly increases. This level of ψ_G cannot be reached experimentally in graphene membrane, as this requires a V_G larger than 2.0 V, which triggers the electrochemical reactions.³³ On the other hand, in an IFET, the electric potential on the pore wall is considerably higher, equivalent to V_G due to the metallic nature of gate electrode (having an infinitely-large quantum capacitance). We therefore conclude that the quantum capacitance-induced nonlinear damping in the surface potential results in the observed salt rejection. Following

the above discussions, we further investigate the physical limits for the biased graphene nanopores. Specifically, the salt rejection characteristics are controlled by: (i) the overlap of EDL inside the nanopore, essentially controlled by two length scales of λ_D and R_G , and (ii) the graphene surface potential ψ_G controlled by V_G following Eq. 7. To this end, we calculate ψ_G as a function of λ_D/R_G and V_G (Fig. 5a). Clearly, when the bulk concentration c_0 increases, a higher V_G is required to reach the same level of ψ_G . Consequently, as revealed in Fig. 5b, the calculated salt rejection factor ξ increases with both λ_D/R_G and V_G , in line with the experimentally observed $\xi - c_0$ dependence. We also find the overall trends for ψ_G and ξ with respect to λ_D/R_G and V_G are very similar. More importantly, based on our theoretical prediction, with $V_G = 1.25$ V and $\lambda_D/R_G = 1.0$, a high value of ξ of > 0.85 can be achieved.

Effects of salt species

Finally, we examine other salt species and compare the degree of salt rejection between experiments and simulations. Fig. 6a presents the measured salt rejection ξ as a function of V_G from at $c_0 = 0.1$ mM, for the seven salt species considered here, including NaCl, LiCl, KCl, MgSO₄, CaCl₂, K₂SO₄, and K₃Fe(CN)₆ (details see Supplementary Section S7

Roman, could you check the value of Debye length K3(Fe(CN)₆ in Table S3? I calculated 12.4 nm

). Similar to the KCl system discussed earlier, the salt rejection was only observed in the positive V_G regime. The degree of salt rejection decreases with the salt valance; for example, the measured ξ values at $V_G = 1.25$ V decreases from > 0.5 for monovalent NaCl to -0.04 for multivalent K₃Fe(CN)₆. This observation is endorsed by our simulations, in which we calculate ξ as a function of V_g using the same setups in simulations (Fig. 6b). The calculated ξ_{\max} values are quantitatively compared with experiments (Fig. 6c), and the same trend is observed. Indeed, because the Debye screening length λ_D decreases with the salt valence, the graphene surface potential appears to decrease in the multivalent salt systems, thereby reducing ξ (see Fig. 5b). The calculated and experimental ξ_{\max} as a function of λ_D are consequently plotted, for the seven salt

species considered here (Fig. 6d). We notice that without any fitting parameters, our theory can predict the experimental values reasonably well. In addition, the $\xi_{\max} - \lambda_D$ dependence is approximately linear, suggesting that the effect of salt diffusivity is negligible. This finding also explains the concentration dependence of ξ_{\max} observed in Fig. 2d, as $\delta_D \propto c_0^{-0.5}$.

Conclusion

In summary, we have presented a comparative experimental and modeling study on macroscopic salt rejection through a sheet of large-area porous graphene under electrostatic gating. We show that due to a small quantum capacitance of double layer graphene, the graphene surface potential is considerably lower than the applied gate voltage. As a result, the subtle redistribution of the electrochemical potentials create new pathways for ionic transport, which in turn lead to a considerably degree of salt rejection. We report a high degree of salt rejection at $V_G = 1.25$ V of up to 55% and 80%, based on our experiments and theoretical predictions, respectively. We demonstrate that the observed salt rejection positively correlates with the Debye screening length that nonlinearly modulates the graphene surface potential and charge density. The experimental results and fundamental principles presented here open an avenue towards realization of atomically thin 2D porous membranes for advanced separation process in electrolyte solutions.

Methods

Graphene synthesis: Graphene was grown in a cold-wall, low-pressure chemical vapor deposition system (BM 4 inch, Aixtron SE) on surface-pretreated copper foil (Alfa Aesar N° 46986). Synthesis was carried out at 950 °C for 3 min using ethylene after 30 min of hydrogen/argon annealing. A first graphene layer was subsequently transferred to a second one to yield double layer graphene using a PMMA transfer method. A glass slide was used as the support for subsequent patterning of the graphene, PMMA was removed using acetone ultrasonication and subsequent isopropanol (IPA) rinsing. The entire process is described in detail in Ref. 23.

Graphene patterning and transfer to PCTE: Spherical block copolymer (s-BCP) based patterning has enabled the manufacturing of perforated graphene membranes having pores in the range of 10 nm to 50 nm on average up to wafer-scale.²³ In brief, s-BCP (polystyrene-block-polymethylmethacrylate, PS-b-PMMA, 195-b-20, Polymer Source Inc, Canada, 1 weight% in anhydrous toluene) is spun from solution and thermally annealed at 220 °C for 6 h in vacuum. Microphase separation of s-BCP leads to distinct phases: the minor phase will form spheres (PMMA) and the major phase will form the matrix (PS). Oxygen plasma (8 , 100 W, 25 mTorr, Oxford Instruments plc) removes the top layer PS from the PMMA spheres, which are subsequently etched in glacial acetic acid to form a porous etch mask directly on top of the double layer graphene. Anisotropic etching using oxygen beam milling (10 s, 100 mA, 600 V acceleration voltage, Oxford IonFab 600) leads to perforation of the underlying graphene through the porous PS mask. Polymer residues are removed by thermal annealing in hydrogen:argon (9:1) at 400 °C. The patterned graphene is transferred to PCTE membranes (hydrophobic, 400 nm pores, from Sterlitech) by baking the PCTE briefly to the perforated graphene at 180 °C followed by a lift-off etch in buffered hydrofluoric acid (BHF) as described by.²³ A schematic of the process is shown in Fig. S1.

Membrane preparation: The ion-diffusion and gating experiments are performed in a custom-made diffusion cell. An initial dip-wetting procedure using ethanol/water 1:1 is performed to wet the membrane, followed by extensive washing and inserting the membrane. The diffusion cell is filled immediately after mounting the membrane with DI water to prevent drying. The ion solution is placed on the HCR side, distilled water on the LCR side, with a volume of 7.33 mL for each cell. Bar-stirrers close to the membrane ensure well-mixed solutions avoiding potential external concentration polarization effects. Water channels in the fixture ensure stable measurement temperatures using a chiller. The temperature for all measurements is kept at 25 °C. A conductivity probe (eDAQ, Pty Ltd., Australia), inserted on the LCR side measures the conductivity, which is recorded with time steps of 2 s. The membrane is kept wet for the entire series of experiments, multiple rinsing steps with DI water are performed after each experiment and change to a different

salt solution. The salt solutions were prepared immediately before the experiments using MilliQ water that was additionally distilled to increase purity level. The distilled water, has a conductivity of 0.0012 mS/cm with a pH of 6.3, no buffer has been used in these experiments. 7 salts were used: KCl, NaCl, LiCl, K_2SO_4 , $CaCl_2$, $MgSO_4$ and $K_3Fe(CN)_6$. The salts were purchased from Sigma Aldrich and used without further purification, salt solutions were prepared by subsequent dilution of a base solution (1 M) to the final concentrations.

Ion diffusion experiments: Baseline measurements were performed using bare PCTE (b-PCTE) by extracting the diffusion rates of 3 measurements and averaging the resulting values (see Supplementary Section 2). For the measurement, DI water was filled on the LCR side, where a 0.1 mM salt solution is placed on the HCR side of the fixture. The conductivity increase was recorded over 1 h before rinsing and replacing both sides with fresh solutions.

Ion gating experiments: The salt rejection behavior of the graphene was characterized using patterned graphene on PCTE (PG-PCTE) in a 3-interval-type measurement based on salt diffusion: 1h per interval with (i) no bias (ii) bias and (iii) no bias, ruling out possible electrochemical effects at the membrane that might mislead interpretation of the conductivity reading. The voltage is applied via copper tape so that the membrane acts as a working electrode (WE). A platinum wire (length 3 cm, diameter 0.6 mm) placed in the low concentration side of the diffusion cell with a distance of ~ 3.5 cm from the PG-PCTE membrane is counter- (CE) and reference electrode (RE) simultaneously, forming effectively a two-electrode setup. An electrochemical workstation (PGSTAT204, Metrohm Autolab S.V.) is used to apply the selected voltage.

Numerical Simulations: Numerical simulations using finite element method (FEM) were carried out using COMSOL Multiphysics 5.3a. A single pore in graphene is simulated, with the horizontal length of the simulation box set to 20 times of the nanopore size. The transport of ionic species was solved by the Nernst-Planck equation, with the electrostatic potential further given by the Poisson equation. Since the surface on graphene cannot be predetermined, we performed all calculations by setting the values of ψ_G . The surface charge of graphene is further extracted and used to reconstruct

the value of actual V_G applied to graphene. We examined the convergence of the solutions by performing simulations with varied mesh sizes. For further details about the simulation setup please refer to Supplementary Section 5.

Acknowledgement

TBD

R.M.W. and H.G.P. acknowledge the support from XXX. T.T. and C.J.S. are grateful for the financial support from the ETH startup funding.

Author Contributions

H.G.P and C.J.S conceived the experiments. R.M.W and K.Y. measured the ion diffusion and gating experiments. T.T performed numerical simulations. All authors contributed to writing and discussion.

References

- (1) Schoch, R. B.; Han, J.; Renaud, P. Transport phenomena in nanofluidics. *Rev. Mod. Phys.* **2008**, *80*, 839–883.
- (2) Karnik, R.; Duan, C.; Castelino, K.; Daiguji, H.; Majumdar, A. Rectification of Ionic Current in a Nanofluidic Diode. *Nano Lett.* **2007**, *7*, 547–551.
- (3) Nam, S.-W.; Rooks, M. J.; Kim, K.-B.; Rossnagel, S. M. Ionic Field Effect Transistors with Sub-10 nm Multiple Nanopores. *Nano Lett.* **2009**, *9*, 2044–2048.

- (4) Heiranian, M.; Farimani, A. B.; Aluru, N. R. Water desalination with a single-layer MoS₂ nanopore. *Nat. Commun.* **2015**, *6*.
- (5) Heerema, S. J.; Dekker, C. Graphene nanodevices for DNA sequencing. *Nat. Nanotechnol.* **2016**, *11*, 127–136.
- (6) Garaj, S.; Liu, S.; Golovchenko, J. A.; Branton, D. Molecule-hugging graphene nanopores. *Proc. Natl. Acad. Sci.* **2013**, *110*, 12192–12196.
- (7) Suk, M. E.; Aluru, N. R. Water Transport through Ultrathin Graphene. *J. Phys. Chem. Lett.* **2010**, *1*, 1590–1594.
- (8) Jiang, D.-e.; Cooper, V. R.; Dai, S. Porous Graphene as the Ultimate Membrane for Gas Separation. *Nano Lett.* **2009**, *9*, 4019–4024.
- (9) Celebi, K.; Buchheim, J.; Wyss, R. M.; Droudian, A.; Gasser, P.; Shorubalko, I.; Kye, J.-I.; Lee, C.; Park, H. G. Ultimate Permeation Across Atomically Thin Porous Graphene. *Science* **2014**, *344*, 289–292.
- (10) Koenig, S. P.; Wang, L.; Pellegrino, J.; Bunch, J. S. Selective molecular sieving through porous graphene. *Nat. Nanotechnol.* **2012**, *7*, 728–732.
- (11) Drahushuk, L. W.; Strano, M. S. Mechanisms of Gas Permeation through Single Layer Graphene Membranes. *Langmuir* **2012**, *28*, 16671–16678.
- (12) Cohen-Tanugi, D.; Grossman, J. C. Water Desalination across Nanoporous Graphene. *Nano Lett.* **2012**, *12*, 3602–3608.
- (13) Suk, M. E.; Aluru, N. R. Ion transport in sub-5-nm graphene nanopores. *J. Chem. Phys.* **2014**, *140*, 084707.
- (14) Cohen-Tanugi, D.; Grossman, J. C. Water permeability of nanoporous graphene at realistic pressures for reverse osmosis desalination. *J. Chem. Phys.* **2014**, *141*, 074704.

- (15) Cohen-Tanugi, D.; Grossman, J. C. Nanoporous graphene as a reverse osmosis membrane: Recent insights from theory and simulation. *Desalination* **2015**, *366*, 59–70.
- (16) O'Hern, S. C.; Jang, D.; Bose, S.; Idrobo, J.-C.; Song, Y.; Laoui, T.; Kong, J.; Karnik, R. Nanofiltration across Defect-Sealed Nanoporous Monolayer Graphene. *Nano Lett.* **2015**, *15*, 3254–3260.
- (17) Surwade, S. P.; Smirnov, S. N.; Vlassioug, I. V.; Unocic, R. R.; Veith, G. M.; Dai, S.; Mahurin, S. M. Water desalination using nanoporous single-layer graphene. *Nat. Nanotechnol.* **2015**, *10*, 459–464.
- (18) Rollings, R. C.; Kuan, A. T.; Golovchenko, J. A. Ion selectivity of graphene nanopores. *Nature Communications* **2016**, *7*, 11408.
- (19) O'Hern, S. C.; Stewart, C. A.; Boutilier, M. S. H.; Idrobo, J.-C.; Bhaviripudi, S.; Das, S. K.; Kong, J.; Laoui, T.; Atieh, M.; Karnik, R. Selective Molecular Transport through Intrinsic Defects in a Single Layer of CVD Graphene. *ACS Nano* **2012**, *6*, 10130–10138.
- (20) Wang, L.; Boutilier, M. S. H.; Kidambi, P. R.; Jang, D.; Hadjiconstantinou, N. G.; Karnik, R. Fundamental transport mechanisms, fabrication and potential applications of nanoporous atomically thin membranes. *Nat. Nanotechnol.* **2017**, *12*, 509–522.
- (21) Surwade, S. P.; Chai, S.-H.; Choi, J.-P.; Wang, X.; Lee, J. S.; Vlassioug, I. V.; Mahurin, S. M.; Dai, S. Electrochemical Control of Ion Transport through a Mesoporous Carbon Membrane. *Langmuir* **2014**, *30*, 3606–3611.
- (22) Li, D.; Müller, M. B.; Gilje, S.; Kaner, R. B.; Wallace, G. G. Processable aqueous dispersions of graphene nanosheets. *Nat. Nanotechnol.* **2008**, *3*, 101–105.
- (23) Choi, K.; Droudian, A.; Wyss, R. M.; Karl-Philipp, S.; Park, H. G. Multifunctional Wafer-Scale Graphene Membranes for Fast Ultrafiltration and High Permeation Gas Separation. *Sci. Adv.* **2018**, *in press*.

- (24) Sun, P.; Zheng, F.; Zhu, M.; Song, Z.; Wang, K.; Zhong, M.; Wu, D.; Little, R. B.; Xu, Z.; Zhu, H. Selective Trans-Membrane Transport of Alkali and Alkaline Earth Cations through Graphene Oxide Membranes Based on Cation- π Interactions. *ACS Nano* **2014**, 8, 850–859.
- (25) Cheng, C.; Jiang, G.; Simon, G. P.; Liu, J. Z.; Li, D. Low-voltage electrostatic modulation of ion diffusion through layered graphene-based nanoporous membranes. *Nat. Nanotechnol.* **2018**, 13, 685–690.
- (26) MacGillivray, A. D. Nernst-Planck Equations and the Electroneutrality and Donnan Equilibrium Assumptions. *J. Chem. Phys.* **1968**, 48, 2903–2907.
- (27) Kilic, M. S.; Bazant, M. Z.; Ajdari, A. Steric effects in the dynamics of electrolytes at large applied voltages. I. Double-layer charging. *Phys. Rev. E* **2007**, 75, 021502.
- (28) Tian, T.; Lin, S.; Li, S.; Zhao, L.; Santos, E. J. G.; Shih, C.-J. Doping-Driven Wettability of Two-Dimensional Materials: A Multiscale Theory. *Langmuir* **2017**, 33, 12827–12837.
- (29) Xia, J.; Chen, F.; Li, J.; Tao, N. Measurement of the quantum capacitance of graphene. *Nat. Nanotechnol.* **2009**, 4, 505–509.
- (30) Dean, C. R.; Young, A. F.; Meric, I.; Lee, C.; Wang, L.; Sorgenfrei, S.; Watanabe, K.; Taniguchi, T.; Kim, P.; Shepard, K. L.; et al., Boron nitride substrates for high-quality graphene electronics. *Nat. Nanotechnol.* **2010**, 5, 722–726.
- (31) Lee, S.-H.; Lee, H.; Jin, T.; Park, S.; Yoon, B. J.; Sung, G. Y.; Kim, K.-B.; Kim, S. J. Sub-10 nm transparent all-around-gated ambipolar ionic field effect transistor. *Nanoscale* **2015**, 7, 936–946.
- (32) Feng, J.; Graf, M.; Liu, K.; Ovchinnikov, D.; Dumcenco, D.; Heiranian, M.; Nandigana, V.; Aluru, N. R.; Kis, A.; Radenovic, A. Single-layer MoS₂ nanopores as nanopower generators. *Nature* **2016**, 536, 197–200.

- (33) Toh, H. S.; Ambrosi, A.; Chua, C. K.; Pumera, M. Graphene Oxides Exhibit Limited Cathodic Potential Window Due to Their Inherent Electroactivity. *J. Phys. Chem. C* **2011**, *115*, 17647–17650.

Figures

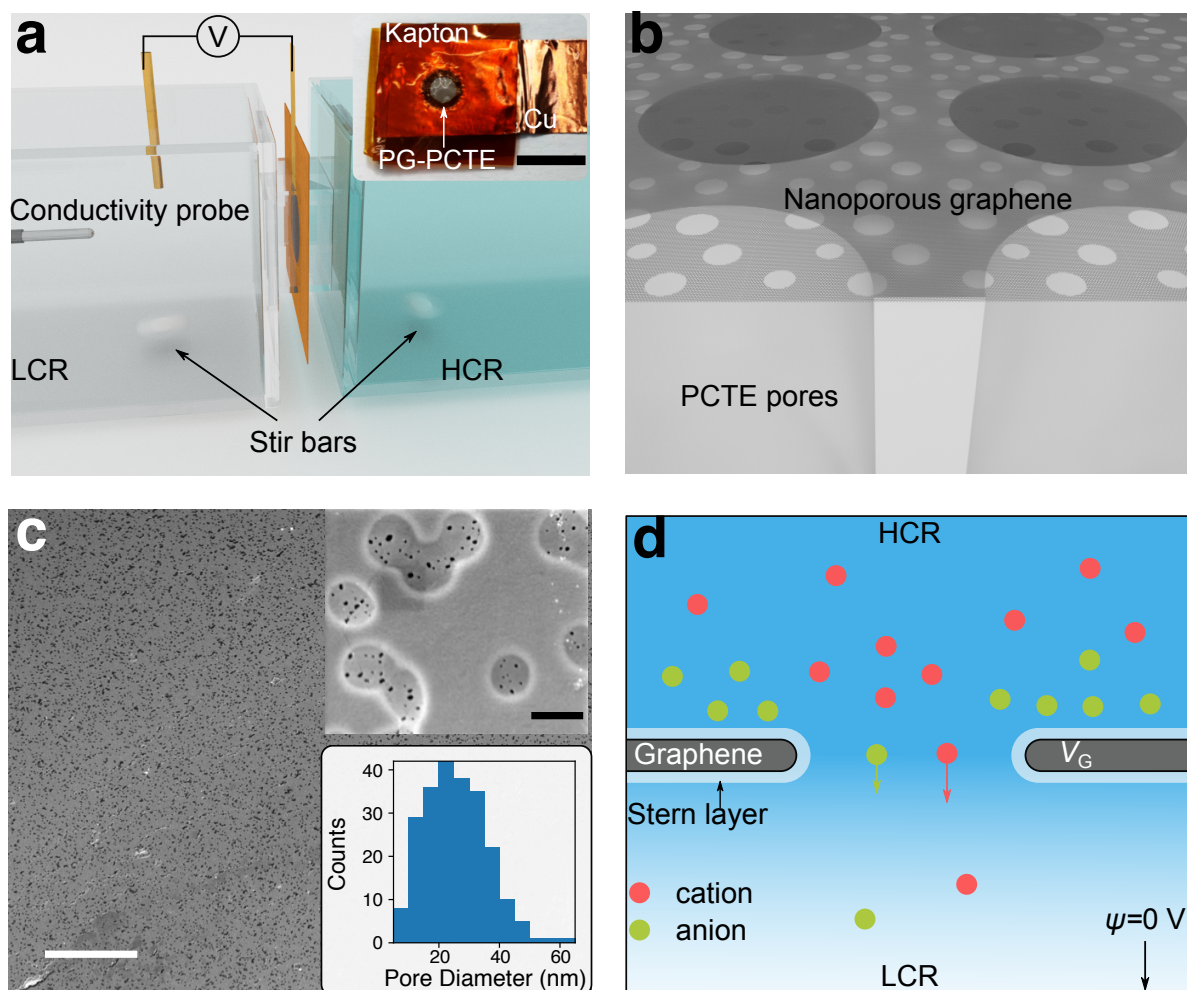


Figure 1: **Experimental setup and nanopore characterization.** **a.** 3D schematic diagram showing the experimental setup. Inset: photograph of the PG-PCTE membrane supported by Kapton and copper tapes, scale bar: 1 cm. **b.** 3D schematic of the nanoscale cross-sectional structure of the PG-PCTE membrane. **c.** SEM image of the PG-PCTE membrane, showing excellent coverage of graphene over the PCTE substrate, scale bar: 20 μm . Upper right inset: high-resolution SEM image of individual nanopores on PG fabricated by the patterning technique, scale bar: 500 nm. Bottom right inset: histogram of the pore diameter distribution revealed by the SEM image. **d.** Schematic of the nanoscale ionic transport through a gated graphene nanopore.

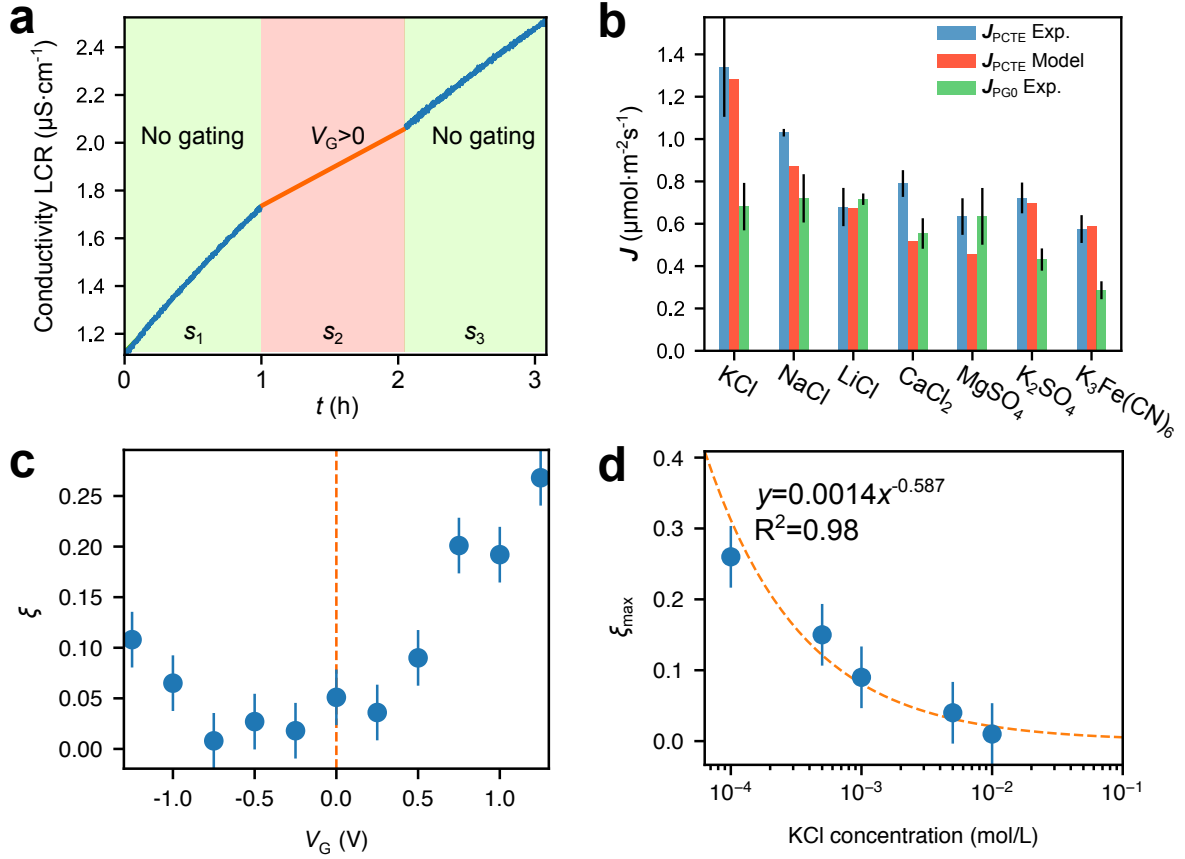


Figure 2: **The experimental evidence of salt rejection.** **a.** Measured conductivity of LCR as a function of time. The slope of conductivity-time curve when $V_G > 0$ is added, is smaller than that without gating. **b.** Molar diffusive flux through bare PCTE (blue bars: experimental; red bars: theoretical values) and PG+PCTE (green bars) membranes for different salts. **c.** Experimentally measured salt rejection factor ξ as a function of V_G for 0.1 mM KCl solution in HCR, showing an asymmetric response, with a higher degree of salt rejection for $V_G > 0$. **d.** ξ_{max} as a function of KCL concentration, fitted by a power law relation, suggesting the effect of Debye length on the observed salt rejection.

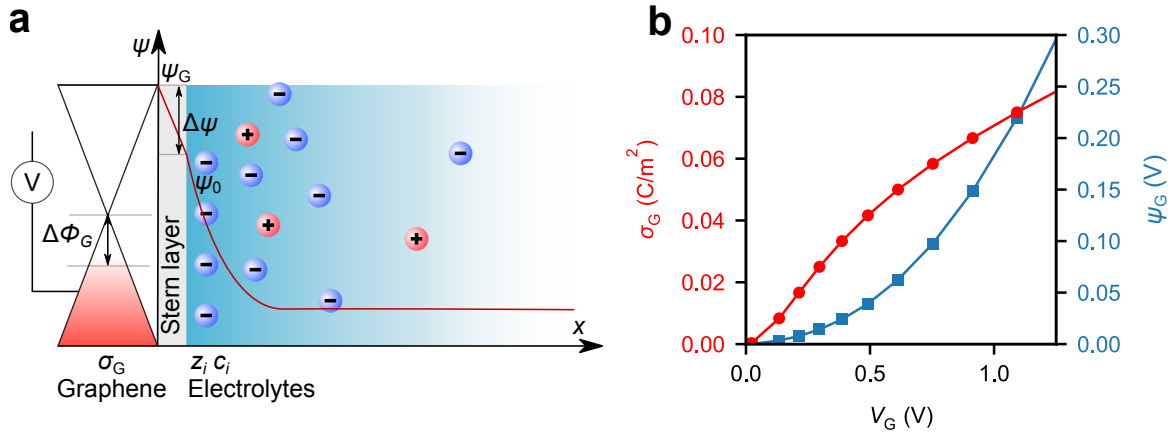


Figure 3: **Interplay between graphene quantum capacitance and EDL.** **a.** Schematic diagram of the electrostatic potential at the graphene-electrolyte interface considering the quantum capacitance of graphene. The interfacial potential of the electrolyte solution, ψ_0 , is smaller than the bias V_G applied, as a result of the change of graphene's Fermi level $\Delta\phi_G$ and the potential drop in the Stern layer $\Delta\psi$. **b.** Calculated surface charge σ_G and surface potential ψ_G of graphene as a function of V_G in a 1 mM KCl solution.

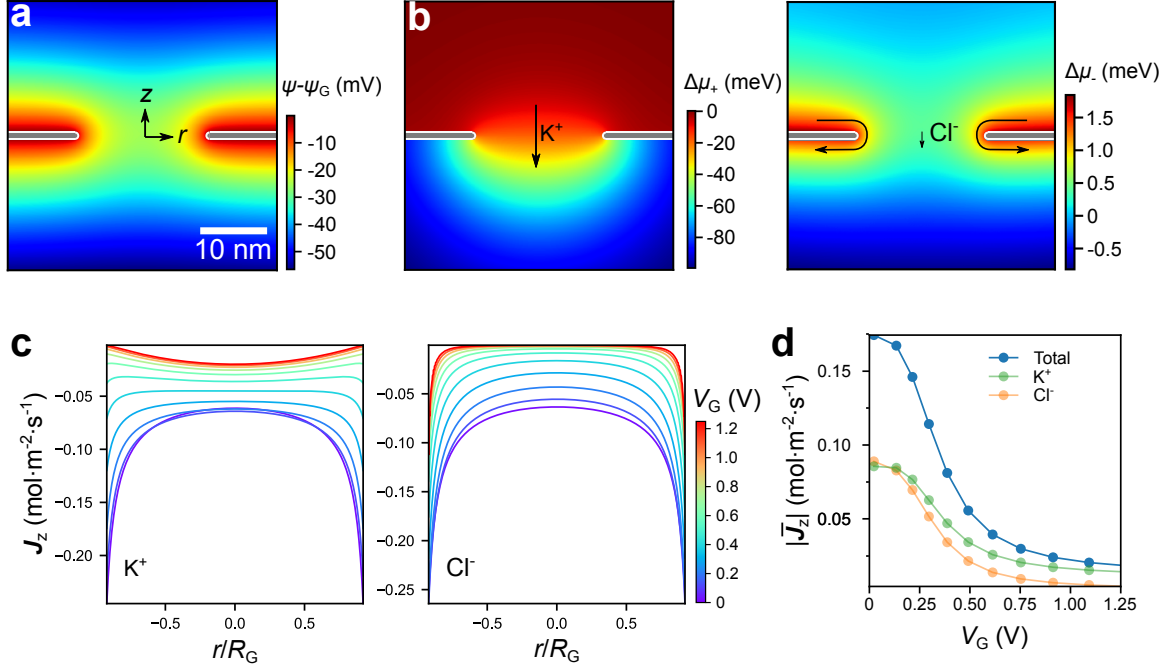


Figure 4: **Self-consistent theoretical calculations.** **a.** Calculated cross-sectional contour plot of electrostatic potential ψ near the center of the graphene nanopore at $V_G = 0.75$ V. **b.** The corresponding electrochemical potential change for cation $\Delta\mu_+$ (left) and anion $\Delta\mu_-$ (right). The reference of electrochemical potential is set in the HCR far from the graphene layer. The diffusive pathways for both ions are indicated by arrows. **c.** Calculated z-component of diffusive fluxes J_z for cation (left) and anion (right) through the pore as functions of the relative position inside the pore, considering different levels of V_G applied. **d.** Calculated z-components of cation, anion, and total fluxes through the graphene nanopore as functions of V_G , showing salt rejection for all fluxes.

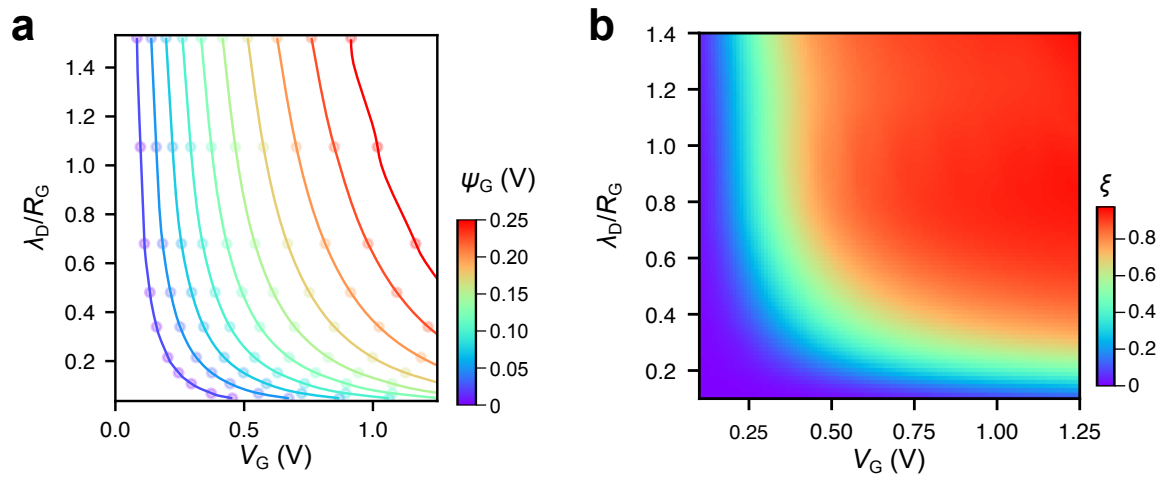


Figure 5: **The Debye length effect.** **a.** Contour plot of the surface potential of graphene ψ_G as a function of λ_D/R_G and V_G . When the Debye length reduces, a higher V_G is required to maintain the same surface ψ_G level. **b.** 2D contour plot of theoretically predicted ξ as a function of λ_D/R_G and V_G . Clearly, a higher degree of salt rejection can be achieved by having a higher V_G and λ_D/R_G ratio.

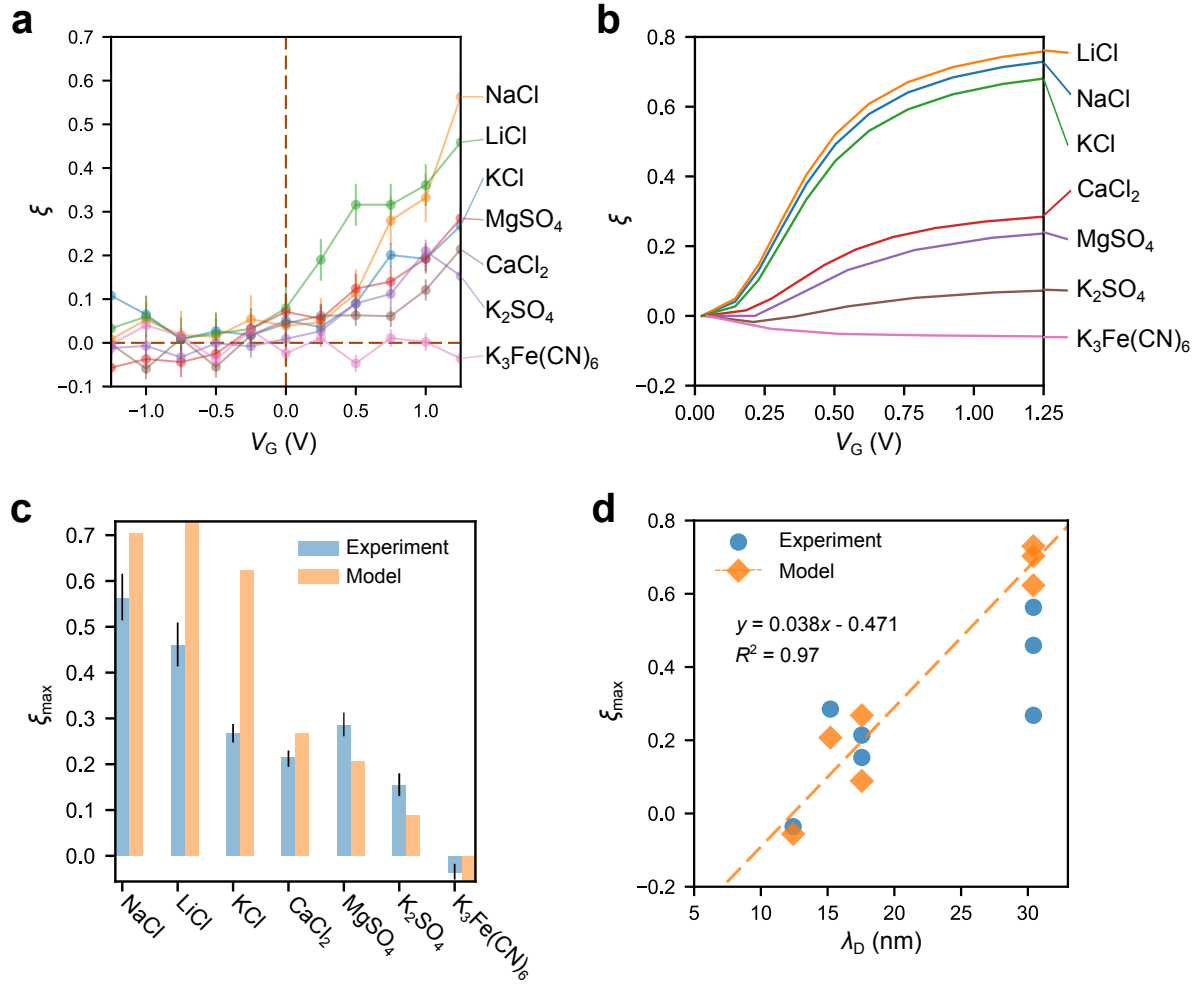


Figure 6: **Comparison between experiments and simulations considering different salt species.** **a.** Experimentally measured ξ as a function of V_G for various salts at 0.1 mM. The error bar indicates the standard error. **b.** Simulated $\xi - V_G$ relations for the salt species considered here. **c.** Comparison between the experimental and calculated ξ_{max} values for different salt species, decreasing with the salt valence. **d.** ξ_{max} as a function of λ_D for the experimental (circle) and model (diamond) values, with a linear correlation.